C Journal of Carbon Research

MDPI

Article

Photoelectrochemical Response of WO_3/Nanoporous Carbon Anodes for Photocatalytic Water Oxidation

Alicia Gomis-Berenguer [1,*], Jesús Iniesta [2], David J. Fermín [3] and Conchi O. Ania [1,*]

1 POR2E Group, CEMHTI, CNRS (UPR 3079), Université d'Orléans, 45071 Orléans, France
2 Institute of Electrochemistry, Faculty of Science, Univ. Alicante, 03080 Alicante, Spain; jesus.iniesta@ua.es
3 School of Chemistry, University of Bristol, Cantocks Close, Bristol BS8 1TS, UK; david.fermin@bristol.ac.uk
* Correspondence: alicia.gomis-berenguer@cnrs-orleans.fr (A.G.-B.); conchi.ania@cnrs-orleans.fr (C.O.A.); Tel.: +33-(0)-238-255-513 (C.O.A.)

Received: 1 June 2018; Accepted: 1 August 2018; Published: 10 August 2018

Abstract: This work demonstrates the ability of nanoporous carbons to boost the photoelectrochemical activity of hexagonal and monoclinic WO_3 towards water oxidation under irradiation. The impact of the carbonaceous phase was strongly dependent on the crystalline structure and morphology of the semiconductor, substantially increasing the activity of WO_3 rods with hexagonal phase. The incorporation of increasing amounts of a nanoporous carbon of low functionalization to the WO_3 electrodes improved the quantum yield of the reaction and also affected the dynamics of the charge transport, creating a percolation path for the majority carriers. The nanoporous carbon promotes the delocalization of the charge carriers through the graphitic layers. We discuss the incorporation of nanoporous carbons as an interesting strategy for improving the photoelectrochemical performance of nanostructured semiconductor photoelectrodes featuring hindered carrier transport.

Keywords: WO_3/nanoporous carbon photoanodes; water oxidation; photoelectrochemistry

1. Introduction

The photoelectrochemical splitting of water to produce oxygen and hydrogen gases is a key process in the development of approaches (e.g., in metal−air batteries and electrochemical water-splitting systems) for the sustainable conversion and storage of renewable energy (e.g., using water and sunlight) [1–3]. The electro and/or photoassisted methods for water splitting are hampered by the low efficiency of the reaction. This is mainly due to the slow kinetics of oxygen evolution and the large overpotentials needed, as well as the stability and performance of most metal oxides usually applied as catalysts (e.g., IrO_2 towards the oxygen evolving reaction (OER) and RuO_2 towards the OER and the hydrogen evolving reaction (HER)) [4–6]. Furthermore, often OER and HER catalysts are not stable under the same pH range. The best performing OER catalysts are in neutral or basic media, whereas the highest efficiencies for HER catalysts are recorded in acidic media. This hinders their integration into photoelectrochemical cells, although recent developments in bipolar membranes have opened new opportunities on this front [7].

Recent research efforts have explored the use of photocatalysts to accelerate the kinetics of both OER and HER [8]. Among different semiconductors, WO_3 is an attractive material for photoelectrochemical water oxidation due to its energetically favorable valence band position (ca. 3.1 V vs. normal hydrogen electrode, NHE), photoactivity under solar light (band gap between 2.4–2.8 eV) and its photostability in acidic medium [9–11]. The conduction band edge is located at around 0.5 V vs. NHE, which is thermodynamically too positive for the non-biased water-splitting reaction; this favors the recombination of the charge carriers, decreasing the conversion efficiency [11–13]. Tungsten trioxide can adopt various crystalline forms (e.g., monoclinic, cubic and hexagonal), with the photochemical and electrochemical properties of this

material governed by its crystalline structure and morphology [14,15]. Among the different crystalline structures of WO_3, the monoclinic and hexagonal phases have been used in photochromic devices [16] and photocatalytic applications [17–19], with the former showing higher stability [20].

The use of carbon nanomaterials has generated interest in the field of photoelectrochemistry as a simple approach to improve the performance of nanostructured photoanodes via: (i) facilitating the transport of majority carriers (electrons); (ii) favoring O_2 adsorption; and (iii) the porosity of the carbon phase [20–24]. Furthermore, metal-free catalysts based on carbon nanomaterials (graphene, carbon nanotubes and nanoporous carbons) have also revealed themselves to be interesting materials with electrocatalytic and photocatalytic activity for the OER [25,26].

In this work, we investigated the effect of nanoporous carbon as an additive to WO_3 particles featuring monoclinic (m-WO_3) and hexagonal (h-WO_3) phases, on their performance in the photoelectrochemical oxidation of water. Carbon materials can promote electron transport by their delocalization in the π-electron density of the graphitic structure; several studies have reported the enhanced photoconversion yields of such semiconductor/carbon catalysts employing a variety of carbons in terms of nature and characteristics ([27–33] and references therein). Hence, various amounts of carbon additive were incorporated to WO_3 photoanodes, assessing the incident photon-to-current efficiency (IPCE) as a function of the applied potential. Electrodes were prepared by adding increasing amounts of a nanoporous carbon of low surface functionalization (ranging from 5–50 wt. %) to WO_3 powders. The carbon additive was chosen based on its photochemical activity under varied illumination conditions [34,35]. The results show a substantial enhancement in the photoelectrochemical responses upon the addition of the nanoporous carbon additive. The data also demonstrated the differing impact of the carbon additive on the photoelectrochemical response of the WO_3, depending on its optical, crystalline, structural and morphological features. This was particularly evident in the case of h-WO_3 nanorods, which exhibited a doubling of the IPCE values.

2. Materials and Methods

2.1. Materials

WO_3 with a hexagonal structure (h-WO_3) was synthesized using a hydrothermal approach as described elsewhere [36]. Briefly, 1.65 g of $Na_2WO_4 \cdot 2H_2O$ were mixed with ca. 0.58 g of NaCl and dissolved into 40 mL of deionized water under magnetic stirring. Upon stirring, a precipitate was formed when excess of 1.5 M HCl was added dropwise to reach a pH 2. Then, the solution was transferred into an autoclave to be heated at 180 °C for 24 h. After cooling to room temperature, the greenish precipitate was washed with ethanol and water several times, and dried at 60 °C overnight. Commercially available WO_3 powders with a monoclinic crystalline structure (m-WO_3) were purchased from Fluka (puriss. 99.9%). A nanoporous carbon obtained by steam activation of bituminous coal was selected as the carbon additive in the preparation of the semiconductor/carbon electrodes (sample referred to as NC). Our previous studies have described the photochemical activity of this carbon material when exposed to light in aqueous medium [35,37]. Details on the characteristics of this material have been discussed in detail elsewhere [34,37]; we herein reintroduce selected textural and chemical properties for data interpretation.

2.2. Preparation of the Electrodes

About 100 mg of solids (either bare WO_3 or WO_3/carbon mixtures) were dispersed in 750 μL of isopropyl alcohol by sonication for 10 min. About 100 μL of the obtained ink were spread onto an FTO (fluorine doped tin oxide)-coated glass slide (surface resistivity ~7 Ω/sq) and spin-coated at 3500 rpm for 30 s. The films were dried at 60 °C for 30 min and annealed at 300 °C for 1 h (heating rate 5 °C/min). The synthesized electrodes were framed to obtain a geometrical area of 1 cm^2. The WO_3/carbon electrodes were labeled as x-W/NCy, where *x* refers to the crystalline phase of WO_3 (m- for monoclinic and h- for hexagonal) and *y* stands for the amount of nanoporous carbon additive, ranging from 5 to 50 wt. %.

2.3. Photoelectrochemical Measurements

The photoelectrochemical measurements were carried out at room temperature in a potentiostat/galvanostat using a cell with an optically flat circular quartz window (diameter 2 cm). A standard three-electrode configuration was used, with a Pt wire counter electrode, Ag/AgCl (KCl saturated) as the reference electrode, and the prepared mixture cast on FTO substrates as photoanodes. The electrodes were immersed in 0.5 M Na_2SO_4 (pH adjusted to 1.3 using H_2SO_4). Transient photocurrent responses were obtained at bias potentials between +0.2 and +0.6 V vs. Ag/AgCl and under several on/off illumination cycles. Dark current equilibrium at the applied potential was allowed before the irradiation. The photoelectrochemical responses were measured several times using various electrodes to evaluate the reproducibility; average values corresponding to at least 3 distinct electrodes are presented. A blue LED (Thorlabs) with a narrow emission centred at 371 nm and photon flux of 3.4×10^{14} cm^{-2} s^{-1} was used as the irradiation source. This was selected considering the absorption features of the semiconductors (see discussion below). The intensity of the LED was calibrated using a standard silicon photodiode (Newport Corporation). The IPCE values were calculated as:

$$\text{IPCE } (\%) = \frac{1240\, j_{ph}}{\lambda P} \times 100$$

where λ (nm) is the wavelength of the monochromatic light irradiating the electrode, and j_{ph} (A/cm^2) corresponds to the stationary photocurrent density measured under illumination with P (W/cm^2) incident irradiation. The number 1240 carries the matching units.

Potentiostatic electrochemical impedance spectroscopy (EIS) measurements were recorded in the frequency range of 0.01 Hz–100 kHz between −0.6 and +0.6 V and using 10 mV AC amplitude. The data obtained were fitted to the Mott–Schottky (MS) equation, which shows the dependence of the interfacial capacitance (C) with the applied potential under depletion conditions.

$$\frac{1}{C_{CS}^2} = \frac{1}{C_H^2} + \frac{2}{\varepsilon\varepsilon_0 e N\left(E - E_{fb} - \frac{kT}{e}\right)}$$

where C_{SC} is the charge space capacity, C_H is the Helmholtz capacity, N is the carrier density (donor N_D or acceptor N_A), ε is the dielectric constant of the electrode material, ε_0 is the electric permittivity of the vacuum, e is the elementary charge, k is the Boltzmann constant, T is the absolute temperature and E_{fb} is the flat band potential.

2.4. Characterization Techniques

The porosity of all samples was determined by N_2 adsorption at −196 °C in a volumetric analyzer. Before the experiments, the samples were outgassed at 120 °C for 17 h under vacuum. The specific surface area (S_{BET}), total pore volume (V_{total}), and the micropore volume (V_{MICRO}) were obtained from the gas adsorption data. UV-Vis diffuse reflectance spectra were recorded on a spectrophotometer equipped with an integrating sphere and using $BaSO_4$ as a blank reference. The band gap energy was calculated from the Tauc plot, using the Kubelka–Munk function from the reflectance measurements. XRD diffractograms were obtained in a Bruker D8 advance instrument operating at 40 kV and 40 mA using Cu kα (λ = 1.5406 nm). Scanning electron microscope (SEM) images were obtained using an FEI QUANTA microscope (FEG 650 model, Thermo Fisher Scientific, Waltham, MA, USA).

3. Results and Discussion

3.1. Characterization of the Materials

Figure 1 shows the XRD patterns and diffuse reflectance spectra of both WO_3 materials used in the fabrication of the photoanodes. The diffractograms confirmed the hexagonal lattice of the semiconductor

prepared by the hydrothermal method [36], with an intense peak at ca. 28.1° characteristic of the 200 direction. All the peaks of the pattern were indexed in the hexagonal structure reported for this material (pattern JCPDS-01-075-2187), with no peaks corresponding to other crystalline phases detected. On the other hand, the commercial powders displayed a monoclinic crystalline structure (JCPDS-01-083-0950 pattern). The mixtures of the semiconductors with the carbon additive were prepared by the physical mixing of the individual components, thus no changes in the crystallinity of the samples were observed (Figure S1). The average crystal size, estimated using the Debye–Scherrer equation, was found to be 27 and 34 nm for the monoclinic and hexagonal phase, respectively. These values are in good agreement with those reported in the literature for a semiconductor synthesized following a similar recipe [38,39].

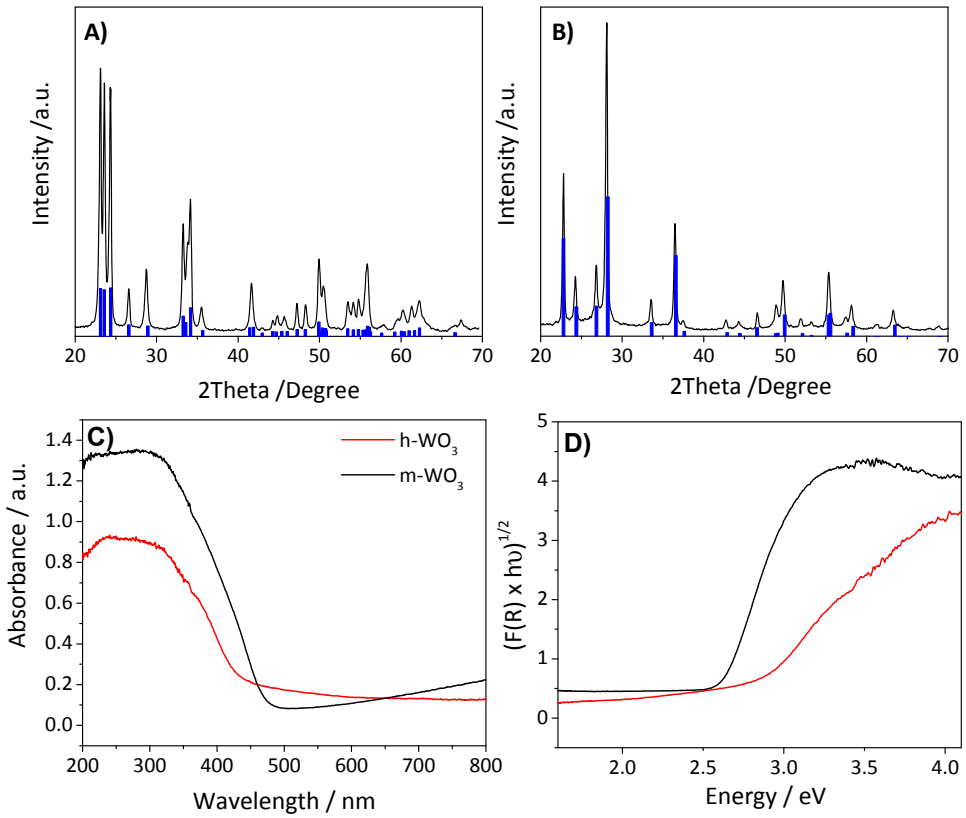

Figure 1. X-ray diffraction pattern of the (**A**) monoclinic and (**B**) hexagonal WO_3. Blue bars indicate the standard patterns (JCPDS-01-075-2187 and JCPDS-01-083-0950 for the hexagonal and monoclinic lattice, respectively); (**C**) Absorbance spectra and (**D**) Tauc representation of hexagonal and monoclinic WO_3.

The light absorption properties of the two phases of WO_3 were measured by UV-Vis spectroscopy and revealed important differences between both materials. Indeed, the spectrum of m-WO_3 presented the characteristic absorption sharp edge at 470 nm (Figure 1C) that corresponds to a band-gap (Eg) of 2.6 eV, as estimated from the Tauc representation in Figure 1D, and in agreement with the values reported in the literature for this material [40–42]. In contrast, the absorption edge corresponding to h-WO_3 shifted slightly towards lower wavelengths (ca. 40 nm), resulting in an optical band gap value of 2.9 eV, also in agreement with the values reported in the literature for the same material [15]. Differences in the band gap for WO_3 have been associated with the presence of cation impurities (W^{4+}, W^{5+}) in the hexagonal phase [17]. The spectra corresponding to the WO_3/carbon mixtures showed similar trends regardless of the crystalline phase of WO_3; below 500 nm the profiles were similar to those of the corresponding bare semiconductor. In the region between 500–800 nm, the absorbance gradually increased with the amount of the carbon additive (Figure S1), as a result of the light absorption of the carbon matrix [43,44].

As for the morphology, Figure 2a–f shows the SEM images of both WO_3 crystalline structures and the carbon additive. The morphology of h-WO_3 is composed of nanorods of uniform sizes (in terms of diameter and length), as opposed to the globular aggregates of nanoparticles of ca. 40–60 nm size observed for m-WO_3. Since the carbon/semiconductor mixtures were prepared by physical mixture, the morphology of the semiconductors was not modified. Additionally, selected SEM images corresponding to the electrodes prepared by spin coating on the FTO support (m-WO_3, h-WO_3, h-W/NC50 and m-W/NC50) are also shown in Figure 2g–l. As shown, the semiconductor particles are homogenously spread throughout the support, with carbon particles randomly dispersed surrounding the semiconductor. It is worth noting that the annealing temperature used for the preparation of the electrodes (ca. 300 °C) was selected to avoid modifications either in the crystallinity of the semiconductor (the phase transition from the hexagonal to the monoclinic phase in WO_3 occurs above 500 °C, see Figure S2) or the composition of the carbon material, which could affect the photoelectrochemical response of the electrodes.

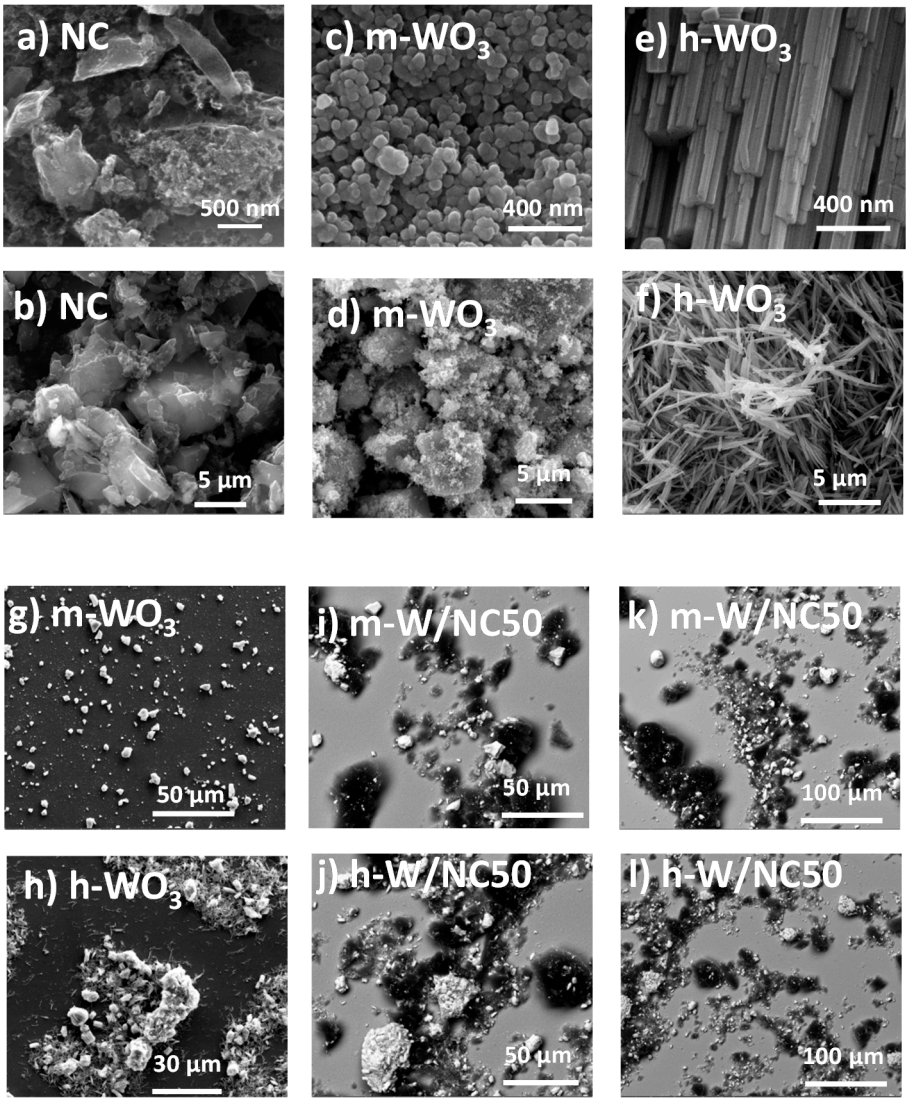

Figure 2. SEM images of (**a**,**b**) the nanoporous carbon additive, (**c**,**d**) monoclinic and (**e**,**f**) hexagonal WO_3, and selected electrodes on the FTO support for (**g**,**h**) the semiconductors and (**i**–**l**) the mixture with 50 wt. % of carbon additive.

Differences between both crystalline phases of WO_3 were also noticed in the porosity. Despite both materials displaying low porosity, the hexagonal phase presented a ca. three times higher surface area

than the monoclinic one (ca. 20 and 6 m^2/g for h-WO_3 and m-WO_3, respectively). The incorporation of the carbon additive increased the surface areas and pore volumes (Figure S3, Table S1), with the values following the stoichiometric trend considering the loading of the semiconductor and the amount of nanoporous carbon (Table S1). On the other hand, both semiconductors showed a somewhat acidic character (slightly more acidic for the monoclinic phase), whereas the WO_3/carbon mixtures presented an increased basic character, inherited from the hydrophobic character of the nanoporous carbon (Table S1).

3.2. Photoelectrochemical Response of the Electrodes

The voltammetric response of the WO_3 electrodes under dark conditions showed that both crystalline phases of WO_3 displayed a similar feature, with the characteristic shape of a semiconductor with two different regions (accumulation and depletion) depending on the bias potential (Figure 3A). The cathodic current observed below 0 V corresponds to the accumulation region of the semiconductor, and is associated with the reversible electrochromic reduction of the material, upon the intercalation of protons from the solution in the electrode surface to form a tungsten bronze ($WO_3 + xH^+ + xe^- \rightarrow H_xWO_3$) [45,46]. Above ca. 0.2 V, the flat current is observed corresponding to the depletion region of the semiconductor. For h-WO_3 the accumulation region appears slightly shifted to more negative potentials (ca. 75–85 mV) compared to m-WO_3. This indicates that the potential of photogenerated electrons in the conduction band of h-WO_3 is more negative than in m-WO_3 (since the onset potential for electron injection in the accumulation region of a semiconductor can be assimilated to the potential of the conduction band edge).

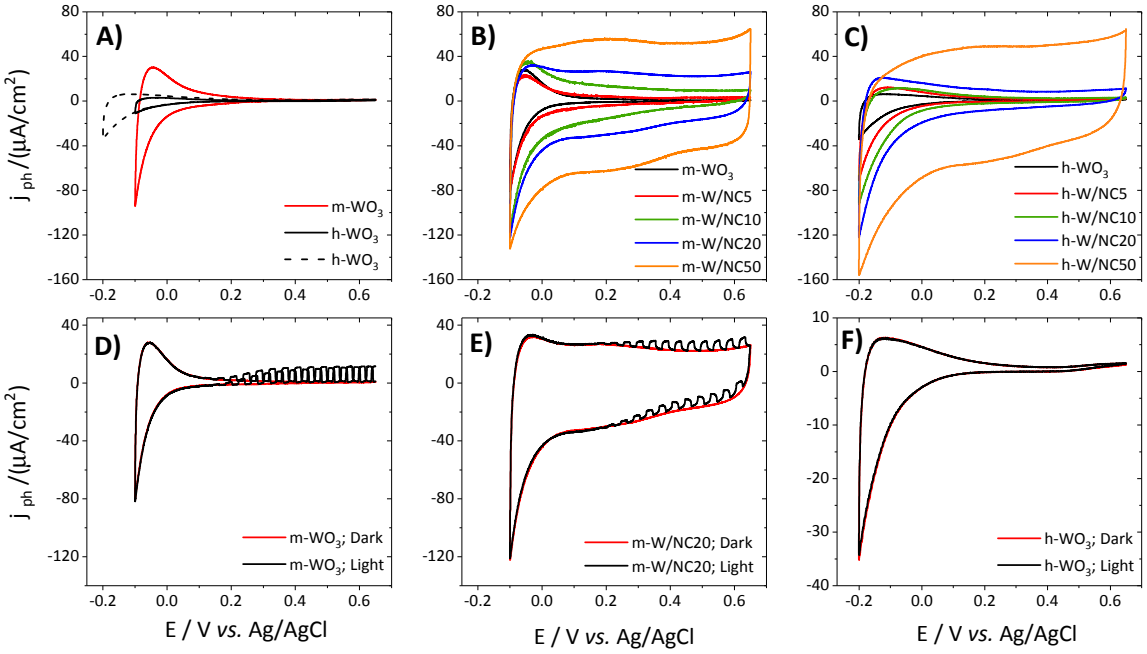

Figure 3. Cyclic voltammograms recorded at 20 mV/s of WO_3 and WO_3/carbon electrodes under (**A**–**C**) dark conditions and (**D**–**F**) and square-wave light perturbation at 371 nm (black line) for selected electrodes: (**D**) m-WO_3, (**E**) m-W/NC20 and (**F**) h-WO_3. For the potentials expressed vs. NHE refer to Figure S4.

For the WO_3/carbon electrodes, the capacitive contribution of the nanoporous carbon was clearly seen in the large dark current densities of the voltammograms as the amount of carbon additive increased (Figure 3B,C). This behavior was expected, considering that the porosity of the WO_3/carbon mixtures increases with the amount of carbon (Table S1).

Upon squared-waved illumination at 371 nm, anodic photocurrents were recorded in the voltammetry profiles for m-WO_3 (Figure 3D,E), as expected for an n-type semiconductor where electrons are the majority charge carriers. They originate from water oxidation in the holes accumulated at the electrode/electrolyte interface, while the electrons travel through the semiconductor to the back contact, driven by the bias potential. The overall photocurrent intensity increases as the potential is swept towards more positive values, which can be phenomenologically rationalized using a decreased interfacial electron density and probability of charge recombination [41,47–49].

In the case of h-WO_3, the cyclic voltammetry under squared-wave illumination showed the same shape as under dark conditions; the lack of photocurrent detection in the voltammetry of the electrodes in the absence of an external potential (Figure 4) indicates a fast recombination of the electron/hole pairs for this material. The drop in the photopotential under open-circuit conditions (Figure S5) confirmed the photoactivity of h-WO_3, as well as its n-type character, similar to m-WO_3. Indeed, the evaluation of the donor density (N_D) in dark conditions with impedance measurements using the Mott–Schottky equation rendered similar values for both crystalline phases of WO_3 (ca. 1.9–3.8 $\times$ 10^{20} cm^{-3}) (Figure S6). These values are in good agreement with those reported in the literature for monoclinic tungsten trioxide [14].

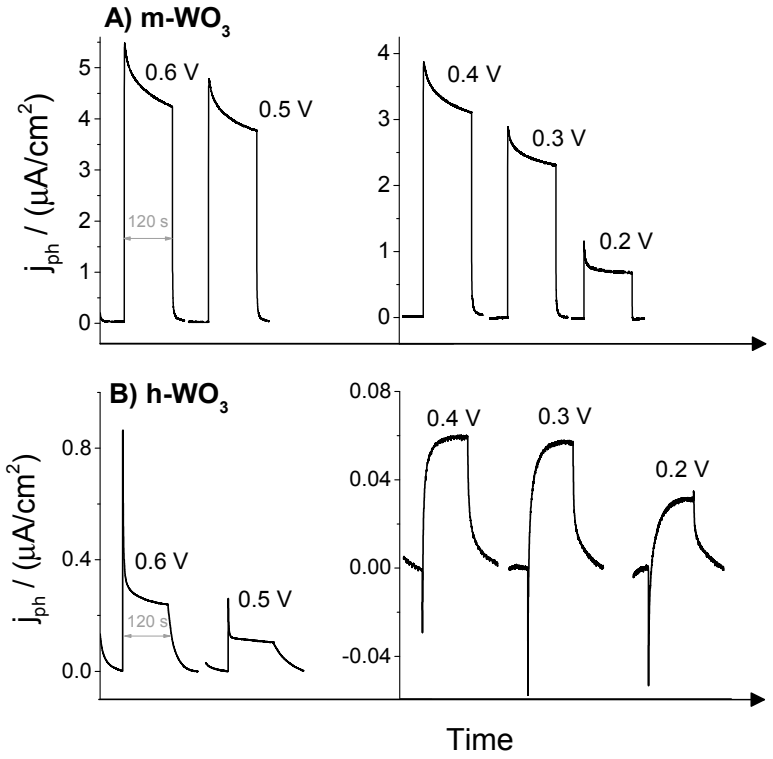

Figure 4. Transient photocurrent responses for (**A**) m-WO_3 and (**B**) h-WO_3 electrodes at various bias potentials between 0.2–0.6 V vs. Ag/AgCl under illumination (2 min) at 371 nm (photon flux of 3.4 $\times$ 10^{14} cm^{-2} s^{-1}).

Despite the similar donor density of both crystalline phases of WO_3, the photocurrent measured for h-WO_3 under squared-wave illumination were smaller than those of m-WO_3, confirming the strong recombination of the charge carriers in the absence of a bias potential. The large capacitive current under dark conditions of the WO_3/carbon electrodes with carbon contents above ca. 20 wt. % hindered the detection of small photoresponses. Thus, transient photocurrent responses at constant potentials were used to assess the photoelectrochemical activity of WO_3 and the WO_3/carbon electrodes between 0.2 and 0.6 V vs. Ag/AgCl (Figure 4). It should be pointed out that above 0 V vs. SCE, the intercalation of protons in the structure to form tungsten bronze is avoided. Furthermore, when tested under

consecutive illumination cycles (Figure S7) similar shape and photocurrent intensities were obtained, confirming the photostability of the electrodes. The photochemical stability of the WO_3 electrodes upon long-term irradiation is in agreement with other studies from the literature [50–53].

The transients of both WO_3 electrodes exhibited the typical shape of an n-type semiconductor, with positive photocurrent values increasing with the applied potential. The photocurrent intensity was an order of magnitude higher for m-WO_3 than for h-WO_3, despite the latter having a higher specific surface area (Table S1). The higher effective absorbance at 371 nm of m-WO_3 (Figure 1C) in comparison to h-WO_3, can contribute to its higher photocurrent. On the other hand, it is also worth noting that previous photochemical and photoelectrochemical studies have concluded that h-WO_3 shows lower activity than m-WO_3 [14,42]. The most remarkable difference between both structures is the shape of the photocurrent transients, particularly at low bias potentials. For m-WO_3, an initial rapid and sharp photocurrent was recorded upon switching on the irradiation, followed by a relaxation to a quasi-stationary state. For some electrodes an anodic current peak (overshoot) was observed after the first seconds of irradiation; however upon switching off the illumination, no negative undershoots were observed at any of the applied potentials, as expected for materials showing surface recombination reactions, which arise from the fact that electron and hole currents have different relaxation times and opposite signs [54]. This behavior was reproducible after successive on/off illumination cycles. On the other hand, the quasi-stationary photocurrent was strongly dependent on the applied potential, which is a clear manifestation of bulk recombination processes. Furthermore, similar photocurrents were obtained by the front- and back-side illumination modes of the electrodes, discarding carrier transport limitations as the main mechanism governing the photocurrent losses [55,56]. This behavior suggests that the undershoots are attributed to the hindered transport of the majority carriers (electrons) under illumination trapped in deep states, which leads to the generation of a time-dependent photovoltage that decreases the effective interfacial potential and increases recombination. Another explanation would be the inactivation of the surface of the electrode due to the products of water oxidation [57].

In the case of h-WO_3, different behavior was obtained depending on the applied potential. At bias potentials of ca. 0.5 and 0.6 V vs. Ag/AgCl, the response is quite similar to that of m-WO_3, although with more pronounced overshoots. At applied potentials between 0.2–0.4 V vs. Ag/AgCl, a negative photocurrent peak appeared instantaneously after switching-on the light, followed by a gradual increase in the anodic photocurrent until a quasi-stationary state value was achieved. After irradiation, the anodic photocurrent slowly returned to the background value (the differences in kinetics were considerable, compared to m-WO_3). Negative instantaneous photocurrents were also observed with the same intensity under de-aerated conditions, discarding the influence of oxygen on the process (results not shown). These unusual bipolar transient responses reveal an instantaneous interfacial charge distribution leading to an excess of electron density upon illumination, equivalent to applying a potential step from positive to negative values. As the photo-transient response relaxes, the faradaic component (water oxidation) takes over, leading to a relaxation of the high photocurrent. A detailed analysis of the nature of the trap states in these complex materials is beyond the scope of this work.

Interestingly, the instantaneous photoresponses in both materials were very different in the case of WO_3/carbon electrodes, pointing to better charge transfer dynamics in the presence of the carbon phase (Figure 5). In the case of m-W/NC electrodes, a significant increase in the photocurrent magnitude in the presence of the carbon additive was observed; however, the main features of the photocurrent transients remained unaffected by the addition of carbon. The same trend was observed for all studied potentials (0.2–0.6 V vs. Ag/AgCl). As we have already reported [58], the larger increase in the photocurrent was obtained for the electrodes with ca. 20 wt. % carbon additive. Nonetheless, the photocurrent values obtained for the electrodes with carbon contents between 5 and 50 wt. % were higher than those of the bare semiconductors, demonstrating that these hybrid electrodes are more photoactive than bare m-WO_3. It should be mentioned that in previous studies, we reported the activity of the nanoporous carbon used herein as the additive for the photoelectrochemical oxidation

of water. The carbon photoanode did not present activity at bias potentials below +0.5 V vs. Ag/AgCl, and the photocurrent values were extremely low compared to those herein reported [26].

In the case of h-W/NC electrodes, the incorporation of the carbon on the electrodes also provoked an increase in the photocurrent when the amount of carbon was higher than 10 wt. % (Figure 5). The increase was more pronounced for low bias potentials, between 0.2–0.4 V vs. Ag/AgCl; in terms of IPCE, the values increased twofold from h-W to h-W/NC10 (Table 1). For carbon amounts between 20–50 wt. %, the photocurrent remained rather constant and was still higher than the value of the semiconductor, indicating that the carbon material was able to somewhat compensate for the lower amount of the semiconductor in measured photocurrents. The fact that the shape of the transients was preserved after the addition of the nanoporous carbon to both crystalline phases indicates that the carbon material does not alter the photoelectrochemical mechanism of the electrodes. This is somewhat expected, since the WO_3/carbon electrodes were prepared by a physical mixture of the semiconductor and the carbon additive.

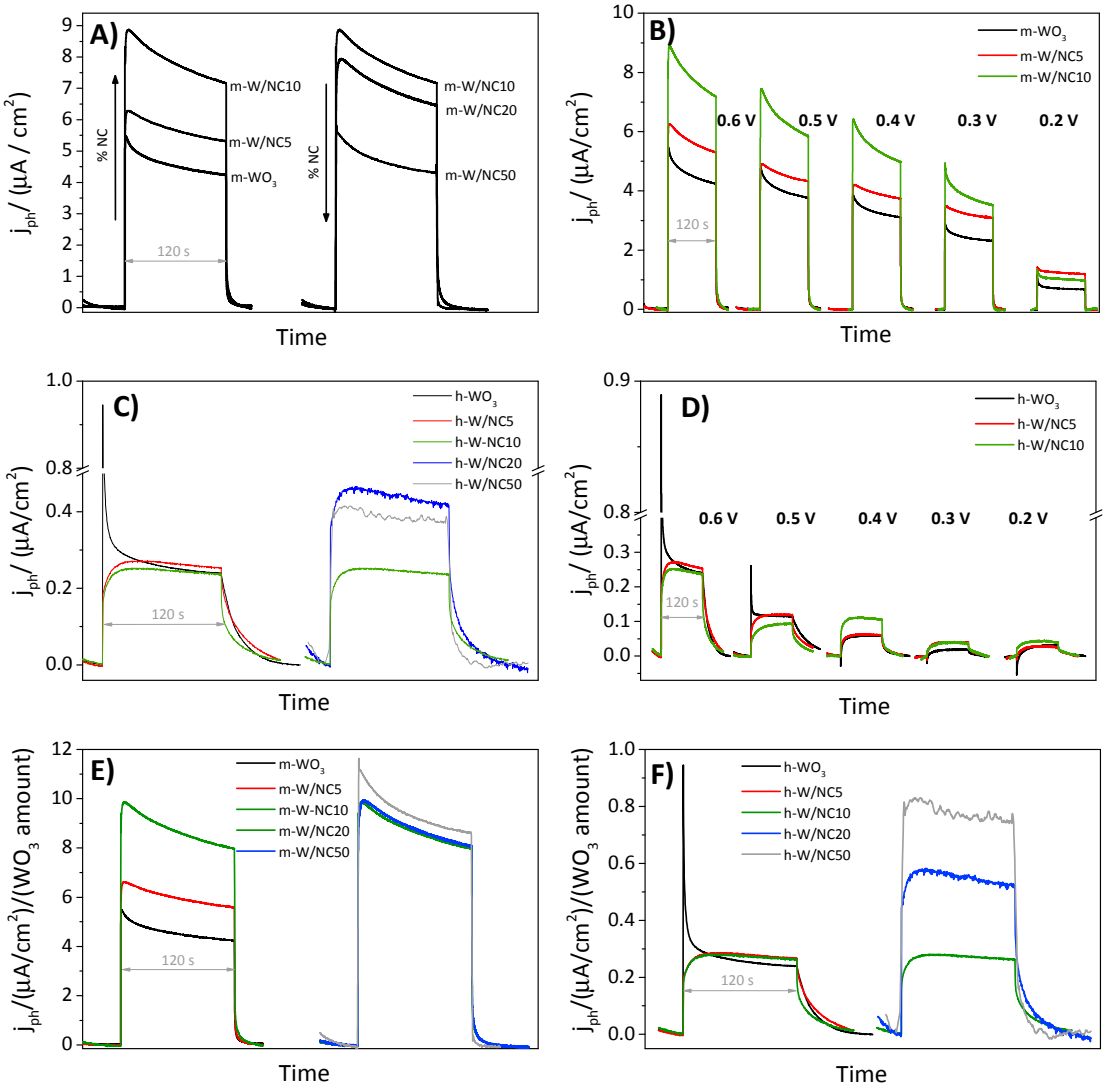

Figure 5. (**A**–**D**) Transient photocurrent responses under illumination (2 min) at 371 nm of the prepared WO_3, and WO_3/carbon electrodes at various bias potentials; (**E**,**F**). Transient photocurrent responses normalized vs. the amount of WO_3 in the electrodes.

Table 1. IPCE values of all studied electrodes at applied potentials between 0.6 and 0.2 V vs. Ag/AgCl.

		h-WO_3					m-WO_3				
		Amount of Nanoporous Carbon (wt. %)									
		0	5	10	20	50	0	5	10	20	50
Potential (V vs. Ag/AgCl)	0.6 V	0.40	0.40	0.44	0.66	0.74	5.88	10.32	13.19	12.58	7.75
	0.5 V	0.30	0.27	0.38	0.60	0.51	5.38	8.95	10.71	9.97	6.22
	0.4 V	0.08	0.12	0.24	0.47	0.27	5.72	7.08	9.32	9.60	4.97
	0.3 V	0.04	0.09	0.18	0.36	0.14	3.41	6.16	6.72	5.31	2.77
	0.2 V	0.02	0.01	0.17	0.11	0.09	1.32	2.63	1.97	1.26	0.55

For both crystalline phases, larger photocurrents and IPCE values were recorded for the electrodes with nanoporous carbon added to the semiconductor, which confirms a more effective charge carrier collection in the presence of the carbon. It should be mentioned that even if these IPCE values are not among the highest reported for other water oxidation photocatalysts, they demonstrate an important increase in the performance of WO_3 upon the incorporation of a metal-free nanoporous carbon in the electrodes. This confirms that the use of porous amorphous carbons is indeed an interesting strategy to improve the performance of semiconductors in the oxygen evolution reaction.

Figure 6 shows a comparison between the photocurrents upon illumination of the both series of electrodes prepared with monoclinic and hexagonal WO_3 at different bias potentials. As seen, notable differences were obtained for both crystalline structures, with photocurrent values of h-WO_3 notably smaller than those of m-WO_3 regardless of the applied potential. The effect of the nanoporous carbon additive appears different for both crystallographic phases of WO_3 (Figure 6). For m-WO_3, a notable increment in the photocurrent was registered (twice the initial value) after the addition of 5 wt. % of nanoporous carbon, with the electrodes with 10–20 wt. % carbon achieving the maximum performance. For the electrodes with carbon content of 50 wt. %, the photocurrent drops considerably, pointing out to some shadowing effects from the carbon additive. In the case of h-WO_3, the enhancement in the photocurrent values was only remarkable for amounts of carbon above 20 wt. %, and the maximum performance was also obtained for higher amounts of carbon for all the bias potentials.

This is most interesting, considering that the amount of semiconductor was gradually reduced as the amount of carbon additive increased (demonstrating that the W/NC electrodes were more efficient than bare WO_3). Indeed, if the photocurrent values were normalized vs. the amount of semiconductor in the mixtures (Figure 5E,F), it was clearly seen that all the W/NC electrodes exhibited a higher photocurrent than the bare semiconductor, even for the electrodes with the largest amount of carbon additive. These results also indicate that the beneficial effect of the nanoporous carbon is more significant for the h-WO_3/carbon mixtures. In the monoclinic phase, similar normalized photocurrents are obtained for the amounts of 10–50 wt. %. However, for the hexagonal phase, the normalized photocurrent at 0.6 V increased remarkably for 10, 20 and 50 wt. % and no plateau was observed. Still, the photocurrent values obtained were much lower than those of the m-WO_3 electrodes, indicating that there were large losses of photogenerated charge carriers for this system, and that additional measures need to be undertaken to improve the photoelectrochemical response of this material (such as using a different carbon additive).

To clarify the role of the carbon additive, several parameters should be considered. First, the carbon matrix could act as an electron acceptor, favoring the diffusion and mobility of the photogenerated electrons via delocalization within the conjugated π-electron density of the graphene-like sheets of carbon. A similar behavior has been reported for hybrid catalysts incorporating carbon nanotubes and graphene as additives to semiconductors [59]. Secondly, due to the hydrophobic nature of the carbon, water molecules are confined (adsorbed) inside the nanopore voids of the carbon, which could influence the activation energy for water oxidation. Thus, the presence of small pores and surface hydrophobicity are important factors to boost the strong adsorption of water molecules in the nanopores to enhance the conversion of water. Finally, it should

also be considered that the nanoporous carbon used in the preparation of the WO_3/carbon electrodes has a certain degree of photoactivity itself [34,35,60] and has shown photoelectrochemical activity for the oxidation of water as a metal-free carbon photoanode. All these processes coexist in these electrodes, contributing to the superior photoelectrochemical activity of the WO_3/carbon electrodes for the water oxidation reaction.

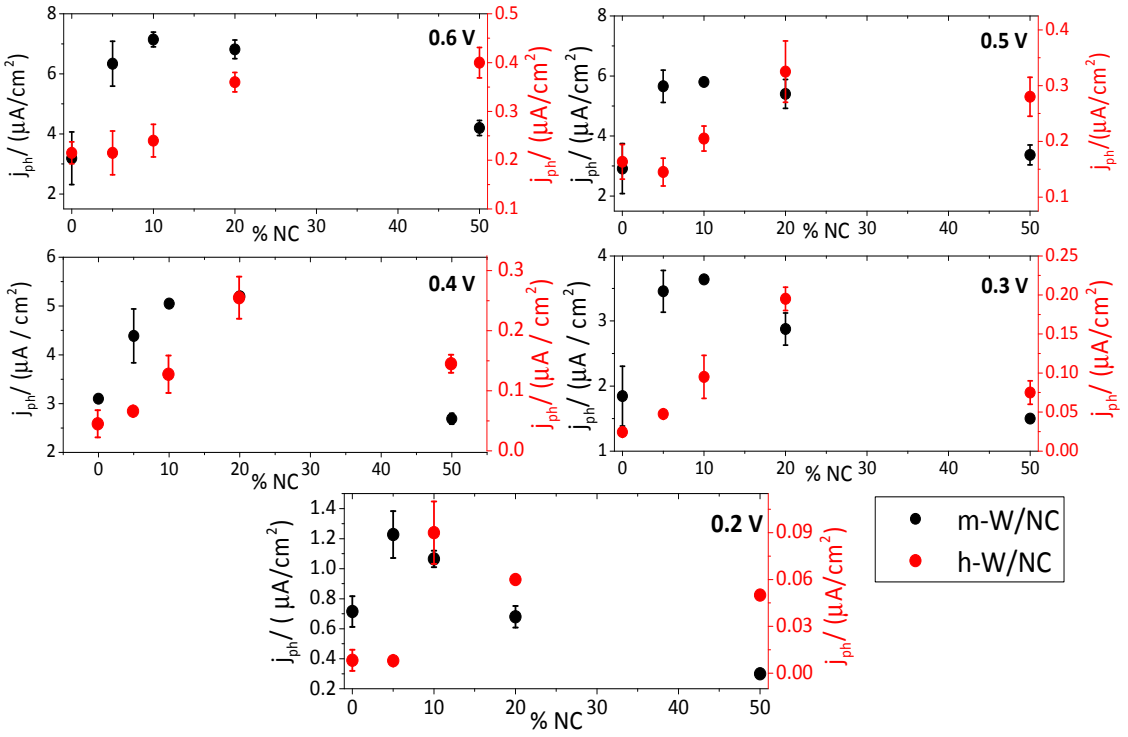

Figure 6. Photocurrent values for m-W/NC (black line) and h-W/NC (red line) electrodes as a function of the amount of nanoporous carbon for various applied potentials.

4. Conclusions

This work provides new insights into the effect of nanoporous carbon additives on the photoelectrochemical activity of monoclinic and hexagonal WO_3 nanoparticles for the photooxidation of water under a potential bias. The data revealed the different photoelectrochemical efficiency of monoclinic and hexagonal WO_3 electrodes for the photooxidation of water, due to a large recombination rate of the photogenerated charge carriers in the latter. The incorporation of increasing amounts of an amorphous nanoporous carbon additive of low functionalization allowed the improvement of the photoelectrochemical efficiency of the electrodes in both cases. The effect of the carbon material was more pronounced in the hexagonal phase of WO_3 (least-performing semiconductor), with about a four-fold increase in the photocurrent of the WO_3/carbon electrodes, and the largest increase in the photocurrent for the electrode with the largest amount of carbon (ca. 50 wt. %). The enhanced photocurrent values obtained for the WO_3/carbon electrodes are attributed to the key features of the carbon and its role in facilitating the majority carrier transport through the graphitic layers. It is also suggested that the porosity of the carbon additive is important to promote water nanoconfinement, which could contribute to a more facile water photo-oxidation. These results demonstrate the possibility of using nanoporous carbons to boost the photoelectrochemical efficiency of a semiconductor with low photochemical activity (i.e., h-WO_3) for the photooxidation of water using UV irradiation. This is an interesting strategy, given the versatility of carbon materials in terms of varied physicochemical features (e.g., porosity, morphology, composition, structure), that would allow for a low-cost approach to optimizing the performance of semiconductor/nanoporous carbons.

Supplementary Materials: The following are available online at http://www.mdpi.com/2311-5629/4/3/45/s1, Figure S1: X-Ray diffraction patterns of (**A**) m-WO_3, NC and the m-WO_3/carbon mixtures; (**B**) h-WO_3, NC and the h-W/NC50, diffractograms are shifted for clarity; red bars indicate the standard pattern (JPDS-01-083-0950 and JCPDS-01-075-2187 corresponding to monoclinic and hexagonal lattice, respectively). Absorbance spectra of (**C**) m-WO_3 and the corresponding m-WO_3/carbon mixtures and (**D**) h-WO_3 and h W/NC50; Figure S2: X-Ray diffraction patterns of h-WO_3 with increasing the calcination temperature; dots indicate the standard patterns corresponding to the hexagonal and monoclinic lattices; Figure S3: Nitrogen adsorption isotherms at −196 °C performed for the nanonoporous carbon and the semiconductor/carbon mixtures analysed (close symbols represent adsorption; empty symbols represent desorption); Figure S4: Cyclic voltammograms recorded at 20 mV/s of WO_3 and WO_3/carbon electrodes under (A–C) dark conditions and (D–F) and square-wave light perturbation at 371 nm (black line) for selected electrodes: (D) m-WO_3, (E) m-W/NC20 and (F) h-WO_3. Potentials are expressed vs. NHE; Figure S5: Evolution of the open-circuit potential (vs. Ag/AgCl) of (**A**) h-WO_3 and (**B**) m-WO_3 electrodes under illumination at 371 nm (photon flux of 3.4×10^{14} cm^{-2} s^{-1}); Figure S6: Mott-Schottky plots of WO_3 at 3.1 kHz under dark conditions in 0.5 M Na_2SO_4 pH 1.3; Figure S7: Consecutive transient photocurrent responses of m-W/NC10 electrode at 0.5 V vs. Ag/AgCl (left). Cyclic voltammetry of m-W fresh and after irradiation (right); Table S1: Main textural parameters of the semiconductors and the semiconductor/carbon mixtures obtained from the equilibrium nitrogen adsorption/desorption isotherms at −196 °C and surface pH.

Author Contributions: A.G.-B., J.I. and C.O.A. conceived and designed the experiments; A.G.-B. performed the experiments; A.G.-B., J.I., D.J.F. and C.O.A. analyzed the data and discussed the results; A.G.-B. and C.O.A. wrote the paper. All authors read and approved the final manuscript.

Funding: This work was funded by the European Council Research through a Consolidator Grant (ERC-CoG-648161, PHOROSOL).

Acknowledgments: European Council Research through a Consolidator Grant (ERC-CoG-648161, PHOROSOL). D.J.F. acknowledges the support by the Engineering and Physical Sciences Research Council (Grant EP/L017792/1).

Conflicts of Interest: The authors declare no conflict of interest.

References

1. Stamenkovic, V.R.; Strmcnik, D.; Lopes, P.P.; Markovic, N.M. Energy and fuels from electrochemical interfaces. *Nat. Mater.* **2017**, *16*, 57–69. [CrossRef] [PubMed]
2. Shaner, M.R.; Atwater, H.A.; Lewis, N.S.; McFarland, E.W. A comparative technoeconomic analysis of renewable hydrogen production using solar energy. *Energy Environ. Sci.* **2016**, *9*, 2354–2371. [CrossRef]
3. Lewis, N.S.; Nocera, D.G. Powering the planet: Chemical challenges in solar energy utilization. *Proc. Natl. Acad. Sci. USA* **2006**, *103*, 15729–15735. [CrossRef] [PubMed]
4. Maeda, K.; Domen, K. Photocatalytic water splitting: Recent progress and future challenges. *J. Phys. Chem. Lett.* **2010**, *1*, 2655–2661. [CrossRef]
5. Botella, P.; García-González, E.; Dejoz, A.; López Nieto, J.M.; Vázquez, M.I.; González-Cablet, J. Selective oxidative dehydrogenation of ethane on MoWTeNbO mixed metal oxide catalysts. *J. Catal.* **2004**, *225*, 428–438. [CrossRef]
6. Abdelouabad, A.L.B.; Roullet, M.; Brun, M.; Burrows, A.; Kiely, C.J.; Volta, J.C.; Abon, M. Surface alteration of (VO)(2)P_2O_7 by alpha-Sb_2O_4 as a route to control then-butane selective oxidation. *Appl. Catal. A Gen.* **2001**, *210*, 121–136. [CrossRef]
7. Chabi, S.; Papadantonakis, K.M.; Lewis, N.S.; Freud, M.S. Membranes for artificial photosynthesis. *Energy Environ. Sci.* **2017**, *10*, 1320–1338. [CrossRef]
8. Zhang, B.; Wang, S.; Fan, W.; Ma, W.; Liang, Z.; Shi, J.; Liao, S.; Li, C. Photoassisted oxygen reduction reaction in H_2-O_2 fuel cells. *Angew. Chem. Int. Ed.* **2016**, *55*, 14748–14751. [CrossRef] [PubMed]
9. Butler, M.A. Photoelectrolysis and physical properties of the semiconducting electrode WO_3. *J. Appl. Phys.* **1977**, *48*, 1914–1920. [CrossRef]
10. Bignozzi, C.A.; Caramori, S.; Cristino, V.; Argazzi, R.; Meda, L.; Tacca, A. Nanostructured photoelectrodes based on WO_3: Applications to photooxidation of aqueous electrolytes. *Chem. Soc. Rev.* **2013**, *42*, 2228–2246. [CrossRef] [PubMed]
11. Liu, X.; Wang, F.; Wang, Q. Nanostructure-based WO_3 photoanodes for photoelectrochemical water splitting. *Phys. Chem. Phys.* **2012**, *14*, 7894–7911. [CrossRef] [PubMed]
12. Zheng, J.Y.; Song, G.; Kim, C.W.; Kang, Y.S. Fabrication of (001)-Oriented monoclinic WO_3 films on FTO substrates. *Nanoscale* **2013**, *5*, 5279–5282. [CrossRef] [PubMed]
13. Liu, Y.; Wygant, B.R.; Mabayoje, O.; Lin, J.; Kawashima, K.; Kim, J.H.; Li, W.; Li, J.; Mullins, C.B. Interface engineering and its effect on WO_3-based photoanode and tandem cell. *ACS Appl. Mater. Interfaces* **2018**, *10*, 12639–12650. [CrossRef] [PubMed]

14. Rodríguez-Pérez, M.; Chacón, C.; Palacios-González, E.; Rodríguez-Gattorno, G.; Oskam, G. Photoelectrochemical water oxidation at electrophoretically deposited WO_3 films as a function of cristal structure and morphology. *Electrochim. Acta* **2014**, *140*, 320–331. [CrossRef]
15. Szilágyi, I.M.; Fórizs, B.; Rosseler, O.; Szegedi, A.; Németh, P.; Király, P.; Tárkányi, G.; Vajna, B.; Varga-Josepovits, K.; László, K.; et al. WO_3 photocatalysts: Influence of structure and composition. *J. Catal.* **2012**, *294*, 119–127. [CrossRef]
16. Wang, S.; Fan, W.; Liu, Z.; Yu, A.; Jiang, X. Advances on tungsten oxide based photochromic materials: strategies to improve their photochromic properties. *J. Mater. Chem. C.* **2018**, *6*, 191–212. [CrossRef]
17. Szilágyi, I.M.; Saukko, S.; Mizsei, J.; Tóth, A.; Madarász, J.; Pokol, G. Gas sensing selectivity of hexagonal and monoclinic WO_3 to H_2S. *Solid States Sci.* **2010**, *12*, 1857–1860. [CrossRef]
18. Wang, N.; Wang, D.; Li, M.; Shi, J.; Li, C. Photoelectrochemical water oxidation on photoanodes fabricated with hexagonal nanoflower and nanoblock WO_3. *Nanoscale* **2014**, *6*, 2061–2066. [CrossRef] [PubMed]
19. Nukui, Y.; Srinivasan, N.; Shoji, S.; Atarashi, D.; Sakai, E.; Miyauchi, M. Vertically aligned hexagonal WO_3 nanotree electrode for photoelectrochemica water oxidation. *Chem. Phys. Lett.* **2015**, 306–311. [CrossRef]
20. Ham, D.J.; Phuruangrant, A.; Thongtem, S.; Lee, J.S. Hydrothermal synthesis of monoclinic WO_3 nanoplates and nanorods used as an electrocatalyst for hydrogen evolution reactions from water. *Chem. Eng. J.* **2010**, *165*, 365–369. [CrossRef]
21. He, Q.; Zhou, F.; Zhan, S.; Huang, N.; Tian, Y. Photoassited oxygen reduction reaction on mpg-C_3N_4: The effects of elements doping on the performance of ORR. *Appl. Surf. Sci.* **2018**, *430*, 325–334. [CrossRef]
22. Zhao, Y.; Nakamura, R.; Kamiya, K.; Nakanishi, S.; Hashimoto, K. Nitrogen-doped carbon nanomaterials as non-metal electrocatalysts for water oxidation. *Nat. Commun.* **2013**, *4*, 2390. [CrossRef] [PubMed]
23. Yeh, T.F.; Chen, S.J.; Yeh, C.S.; Teng, H. Tuning the electronic structure of graphite oxide through ammonia treatment for photocatalytic generation of H_2 and O_2 from water splitting. *J. Phys. Chem. C* **2013**, *117*, 6516–6524. [CrossRef]
24. Xu, Y.; Kraft, M.; Xu, R. Metal-free carbonaceous electrocatalysts and photocatalysts for water splitting. *Chem. Soc. Rev.* **2016**, *45*, 3039–3052. [CrossRef] [PubMed]
25. Ania, C.O.; Seredych, M.; Rodriguez Castellon, E.; Bandosz, T.J. Visible light driven photoelectrochemical water splitting on metal free nanoporous carbon promoted by chromophoric functional groups. *Carbon* **2014**, *79*, 432–441. [CrossRef]
26. Gomis-Berenguer, A.; Velo-Gala, I.; Rodriguez-Castellón, E.; Ania, C.O. Surface modification of a nanoporous carbon photoanode upon irradiation. *Molecules* **2016**, *21*, 1611. [CrossRef] [PubMed]
27. Huang, C.; Chen, C.; Zhang, M.; Lin, L.; Ye, X.; Lin, S.; Markus Antonietti, M.; Wang, X. Carbon-Doped BN nanosheets for metal-free photoredox catalysis. *Nat. Commun.* **2015**, *6*, 7698. [CrossRef] [PubMed]
28. Zhang, G.; Zang, S.; Wang, X. Layered $Co(OH)_2$ deposited polymeric carbon nitrides for photocatalytic water oxidation. *ACS Catal.* **2015**, *5*, 941–947. [CrossRef]
29. Leary, R.; Westwood, A. Carbonaceous nanomaterials for the enhancement of TiO_2 photocatalysis. *Carbon* **2011**, *49*, 741–772. [CrossRef]
30. Faria, J.L.; Wang, W. *Carbon Materials for Catalysis*; Serp, P., Figueiredo, J.L., Eds.; John Wiley & Sons: New York, NY, USA, 2009; Chapter 13; pp. 481–506.
31. Matos, J.; Laine, J.; Herrmann, M. Synergy effect in the photocatalytic degradation of phenol on a suspended mixture of titania and activated carbon. *Appl. Catal. B Environ.* **1998**, *18*, 281–291. [CrossRef]
32. Haro, M.; Velasco, L.F.; Ania, C.O. Carbon-Mediated photoinduced reactions as a key factor in the photocatalytic performance of C/TiO_2. *Catal. Sci. Technol.* **2012**, *2*, 2264–2272. [CrossRef]
33. Zheng, Y.; Lin, L.; Wang, B.; Wang, X. Graphitic carbon nitride polymers toward sustainable photoredox catalysis. *Angew. Chem. Int. Ed.* **2015**, *54*, 12868–12884. [CrossRef] [PubMed]
34. Velasco, L.F.; Fonseca, I.M.; Parra, J.B.; Lima, J.C.; Ania, C.O. Photochemical behaviour of activated carbons under UV irradiation. *Carbon* **2012**, *50*, 249–258. [CrossRef]
35. Velasco, L.F.; Gomis-Berenguer, A.; Lima, J.C.; Ania, C.O. Tuning the surface chemistry of nanoporous carbons for an enhanced nanoconfined photochemical activity. *ChemCatChem* **2015**, *7*, 3012–3319. [CrossRef]
36. Wang, J.; Khoo, E.; See Lee, P.; Ma, J. Synthesis, assembly, and electrochromic properties of uniform crystalline WO_3 nanorods. *J. Phys. Chem. C* **2008**, *112*, 14306–14312. [CrossRef]
37. Velasco, L.F.; Lima, J.C.; Ania, C.O. Visible-light photochemical activity of nanoporous carbons under monochromatic light. *Angew. Chem. Int. Ed.* **2014**, *53*, 4146–4148. [CrossRef] [PubMed]
38. Shen, Y.; Pan, L.; Ren, Z.; Yang, Y.; Xiao, Y.; Li, Z. Nanostructured WO_3 films synthesized on mica substrate with novel photochromic properties. *J. Alloys Compd.* **2016**, *657*, 450–456. [CrossRef]

39. Ramkumar, S.; Rajarajan, G. Effect of Fe doping on structural, optical and photocatalytic activity of WO_3 nanostructured thin films. *J. Mater. Sci. Mater. Eelctron.* **2016**, *27*, 1847–1853. [CrossRef]
40. Nosaka, Y.; Takahashi, S.; Sakamoto, H.; Nosaka, A.Y. Reaction mechanism of Cu(II)-grafted visible-light responsive TiO_2 and WO_3 photocatalysts studied by means of ESR spectroscopy and chemiluminescence photometry. *J. Phys. Chem. C* **2011**, *115*, 21283–21290. [CrossRef]
41. Kumar, S.G.; Rao, K.S.R.K. Tungsten-Based nanomaterials (WO_3 & Bi_2WO_6): Modifications related to charge carrier transfer mechanisms and photocatalytic applications. *Appl. Surf. Sci.* **2015**, *355*, 939–958. [CrossRef]
42. Kalanur, S.S.; Hwang, Y.J.; Chae, S.Y.; Joo, O.S. Facile growth of aligned WO_3 nanorods on FTO substrate for enhanced photoanodic water oxidation activity. *J. Mater. Chem. A* **2013**, *1*, 3479–3488. [CrossRef]
43. Araña, J.; Doña-Rodriguez, J.M.; Tello Rendón, E.; Garriga i Cabo, C.; González-Diaz, C.; Herrera-Melián, J.A.; Pérez-Peñ, A.J.; Colón, G.; Navío, J.A. TiO_2 activation by using activated carbon as a support: Part II. Photoreactivity FTIR study. *Appl. Catal. B Environ.* **2003**, *44*, 153–160. [CrossRef]
44. Carmona, R.J.; Velasco, L.F.; Hidalgo, M.C.; Navío, J.A.; Ania, C.O. Boosting the visible-light photoactivity of Bi_2WO_6 using acidic carbon additives. *Appl. Catal. A Gen.* **2015**, *505*, 467–477. [CrossRef]
45. Bedja, I.; Hotchandani, S.; Kamat, P.V. Photoelectrochemistry of quantized WO_3 colloids. Electron storage, electrochromic, and photoelectrochromic effects. *J. Phys. Chem.* **1993**, *97*, 11064–11070. [CrossRef]
46. Granqvist, C.G. Electrochromic tungsten oxide films: Review of progress 1993–1998. *Sol. Energy Mater. Sol. Cells* **2000**, *60*, 201–262. [CrossRef]
47. Bard, A.J. Photoelectrochemistry and heterogeneous photocatalysis at semiconductors. *J. Photochem.* **1979**, *10*, 59–75. [CrossRef]
48. Celorrio, V.; Bradley, K.; Weber, O.J.; Hall, S.R.; Fermín, D.J. Photoelectrochemical Properties of $LaFeO_3$ Nanoparticles. *ChemElectroChem* **2014**, *1*, 1667–1671. [CrossRef]
49. Peter, L.M.; Ponomarev, W.A.; Fermín, D.J. Intensity-Modulated photocurrent spectroscopy: Reconciliation of phenomenological analysis with multistep electron transfer mechanisms. *J. Electroanal. Chem.* **1997**, *427*, 79–96. [CrossRef]
50. Li, S.; Shelar, D.P.; Hou, C.-C.; Chen, Q.-Q.; Deng, P.; Chen, Y. WO_3 nanospheres with improved catalytic activity for visible light induced cross dehydrogenative coupling reactions. *J. Photochem. Photobiol. A* **2018**, *363*, 44–50. [CrossRef]
51. Kalanur, S.S.; Duy, L.T.; Seo, H. Recent progress in photoelectrochemical water splitting activity of WO_3 photoanodes. *Top. Catal.* **2018**, *61*, 1043–1076. [CrossRef]
52. Han, X.; Xu, D.; An, L.; Hou, C.; Li, Y.; Zhang, Q.; Wang, H. WO_3/g-C_3N_4 two-dimensional composites for visible-light driven photocatalytic hydrogen production. *Int. J. Hydrogen Energy* **2018**, *43*, 2264–2272. [CrossRef]
53. Kwong, W.L.; Nakaruk, A.; Koshy, P.; Sorrell, C.C. Photoelectrochemical properties of WO_3 nanoparticulate thin prepared by carboxylic acid-assisted electrodeposition. *Thin Solid Films* **2013**, *544*, 191–196. [CrossRef]
54. Peter, L.M. Dynamic aspects of semiconductor photoelectrochemistry. *Chem. Rev.* **1990**, *90*, 753–769. [CrossRef]
55. Leempoel, P.; Fan, F.R.F.; Bard, A.J. Semiconductor electrodes. 50. Effect of mode of illumination and doping on photochemical behavior of phthalocyanine films. *J. Phys. Chem.* **1983**, *87*, 2948–2955. [CrossRef]
56. Xiao, S.; Chen, H.; Yang, Z.; Long, X.; Wang, Z.; Zhu, Z.; Qu, Y.; Yang, S. Origin of the different photoelectrochemical performance of mesoporous $BiVO_4$ photoanodes between the $BiVO_4$ and the FTO side Illumination. *J. Phys. Chem. C* **2015**, *119*, 23350–23357. [CrossRef]
57. Monllor-Satoca, D.; Gómez, R. A photoelectrochemical and spectroscopic study of phenol and catechol oxidation on titanium dioxide nanoporous electrodes. *Electrochim. Acta* **2010**, *55*, 4661–4668. [CrossRef]
58. Gomis-Berenguer, A.; Celorrio, V.; Iniesta, J.; Fermin, D.J.; Ania, C.O. Nanoporous carbon/WO_3 anodes for an enhanced water photooxidation. *Carbon* **2016**, *108*, 471–479. [CrossRef]
59. Fu, L.; Xia, T.; Zheng, Y.; Yang, J.; Wang, A.; Wang, Z. Preparation of WO_3-reduced graphene oxide nanocomposites with enhanced photocatalytic property. *Ceram. Int.* **2015**, *41*, 5903–5908. [CrossRef]
60. Gomis-Berenguer, A.; Iniesta, J.; Moro, A.; Maurino, V.; Lima, J.C.; Ania, C.O. Boosting visible light conversion in the confined pore space of nanoporous carbons. *Carbon* **2016**, *96*, 98–104. [CrossRef]